

Nonsymmorphic symmetry-enforced hourglass fermions and Rashba-Dresselhaus interaction in BiInO₃

Ramsamoj Kewat* and Nirmal Ganguli†

Department of Physics, Indian Institute of Science Education and Research Bhopal, Bhauri, Bhopal 462066, India

(Dated: 27 June 2025)

In this study, we investigate the spin texture of the hourglass fermions band network in BiInO₃ using density functional theory (DFT) and symmetry analysis. Hourglass fermions are of interest in spintronics due to their unique and robust band structure, as well as their potential applications in novel electronic devices. BiInO₃ exhibits non-symmorphic crystal symmetries, such as glide reflection and glide rotational symmetry, influencing its electronic properties. Through symmetry analysis, we explore the band crossings and spin textures along specific high-symmetry paths in the Brillouin zone. Our results reveal a fascinating hourglass-shaped band dispersion and spin polarisation governed by symmetry operations and spin-orbit interaction. We analyse the spin-splitting mechanisms, including Dresselhaus and Rashba spin-orbit interactions, and suggest potential applications for spin-based devices. This study sheds light on the role of symmetry in crystals for fascinating spin properties of hourglass fermions in non-symmorphic materials, offering insights for future developments in spintronics.

I. INTRODUCTION

In recent years, there has been a paradigm shift in electronic device fabrication, moving away from traditional charge-based systems towards the promising realm of Spintronics. Unlike conventional electronics that depend on manipulating electronic charges, Spintronics exploits the intrinsic quantum-mechanical property of electron spin. In Spintronics, materials with remarkable quantum effects, such as Spin-Orbit Interaction (SOI), symmetry, topology, and dimensionality, play essential roles. Topological insulators[1–5], Hourglass fermions[6–9], Weyl semimetals[10–14], and superconductors[4, 15] are notable among these materials, offering unique opportunities for novel device architectures and functionalities. Spatial symmetry plays a crucial role in classifying materials with band topology. The crystal symmetry will differentiate the materials, whether it is symmorphic or non-symmorphic. Materials with only point group symmetry are symmorphic and those with glide reflection or screw rotation symmetry are non-symmorphic. The non-primitive translation along with rotational or mirror symmetry in non-symmorphic crystals leads to an hourglass cone-shaped band first predicted theoretically for the (010) surface of the KHgX(X=As, Sb, Bi) family [6] and then studied experimentally by angle-resolved photoemission Spectroscopy (ARPES)[16]. However, later on, many researchers found several hourglass fermions in 3D and 2D materials[8, 9]. Non-symmorphic material inherently has bulk asymmetry, which opens the path to exploring interesting spin textures that might be present in them. The spin-orbit interaction (SOI) in condensed matter physics proposed by Dresselhaus[17] and Rashba [18–21] gives an insight into the novel properties of materials such as momentum-dependent band splitting and

spin-momentum locking. Dresselhaus SOI manifests in materials lacking bulk inversion symmetry, giving rise to a unique momentum-dependent magnetic field $\vec{B} = \alpha(k_y, k_x)$ acting on electron spins. Conversely, Rashba SOI emerges at material surfaces or interfaces having a momentum-dependent magnetic field $\vec{B} = \beta(k_y, -k_x)$ on the electron. These interactions lead to a chiral spin texture in the electronic band structure, a crucial characteristic exploited in the design of spin field-effect transistors (spin FETs)[22]. The momentum-dependent shape of spin has some challenges and limitations in spintronics device applications. One of the challenging issues is related to spin lifetime, which is dictated by the scattering of spins due to impurities and defects within the material. This leads to rapid spin relaxation, known as Dyakonov-Perel spin relaxation[23]. This phenomenon significantly affects the practical realisation and application of spin FETs. To overcome these limitations and unlock Spintronics's full potential, researchers actively seek materials exhibiting a non-chiral or momentum-independent spin texture in their electronic band structure. Such materials, characterised by equal Rashba and Dresselhaus SOI strengths, are termed Persistent Spin Textures (PSTs)[24–26]. By having unique properties of PST materials, it becomes possible to overcome the challenges associated with spin relaxation, paving the way for developing highly efficient and reliable spin-based electronic devices. While exploring non-symmorphic material, BiInO₃ is a good candidate for hourglass fermions with unique PST spin texture due to the presence of a glide mirror and glide rotational symmetry. The following section will discuss a detailed study of its band structure and spin texture using the DFT method and symmetry analysis.

II. CRYSTAL STRUCTURE AND METHOD

BiInO₃ crystallises into a non-centrosymmetric polar orthorhombic crystal with space group $Pna2_1$ (#33) [27].

* Email: ramsamoj18@iiserb.ac.in

† Email: NGanguli@iiserb.ac.in

Besides the identity, the space group comprises only three symmetry operations, namely, a twofold screw rotation about the z -axis \tilde{C}_{2z} ($\{2_{001}|0\ 0\ \frac{1}{2}\}$ in Seitz notation), a glide reflection about the $x = 0$ plane \tilde{M}_x ($\{m_{100}|\frac{1}{2}\ \frac{1}{2}\ \frac{1}{2}\}$ in Seitz notation), and a glide reflection about the $y = 0$ plane \tilde{M}_y ($\{m_{010}|\frac{1}{2}\ 0\ \frac{1}{2}\}$ in Seitz notation), a glide reflection about the $x = 0$ plane \tilde{M}_x ($\{m_{010}|\frac{1}{2}\ \frac{1}{2}\ 0\}$ in Seitz notation). The non-centrosymmetric polar space group allows for a substantial electric polarisation along the z -direction, assisted by the displacement of the heavy Bi and In ions and distorted Bi and In octahedra. The distortion of these octahedra results in an unequal bond length of Bi-O and In-O as shown in Fig. 1. The Bi-O bond length ranges from 2.319Å to 2.809Å, and the In-O bond length ranges from 2.177Å to 2.317Å. The distorted octahedral and non-uniform bond length of Bi-O and In-O results in BiO and InO₂ plane displacement along the z -direction. The planar distance between BiO and InO₂ plane is alternately 2.345 Å and 1.847 Å. Since the BiO plane carries a unit positive charge and InO₂ carry a unit negative charge, the planar displacement causes an asymmetrical distribution of charges and results in an internal electric field along the z -direction.

The electronic structure calculations presented here are performed using density functional theory (DFT) within the framework of the projector augmented wave (PAW) method [28] along with a plane wave basis set, as implemented in the VASP code [29, 30]. A 500 eV plane wave energy cutoff is used for expanding the wavefunctions. An approximate form of the exchange-correlation functional through the generalised gradient approximation due to Perdew, Burke, and Ernzerhof (PBE) [31] is used for the calculations. A $11 \times 13 \times 9$ Γ -centered k -mesh centred at the Γ -point is used for the Brillouin zone integration within the corrected tetrahedron method [32] for the calculations, respectively. The crystal structure is optimised to find atomic positions with Hellmann-Feynman force on each atom below a threshold of 10^{-2} eV/Å and the lattice vectors with minimum stress. The electric polarisation is calculated using the full potential linear augmented plane wave (FP-LAPW) method, as implemented in the WIEN2k code [33], and the BerryPI code [34] interfaced with the WIEN2k code.

III. RESULTS AND DISCUSSIONS

A. Symmetries in BiInO₃

Materials that exhibit symmetry-enforced band crossings possess distinctive characteristics within topological materials. Notably, these band crossings are persistent in the presence of specific symmetries inherent in the material, but they remain susceptible to movement under certain conditions. The mobility of these band crossings primarily arises from Nonsymmorphic crystal symmetries and non-spatial symmetries.

Nonsymmorphic crystal symmetry, denoted as $\mathcal{G} = \{g, t\}$, is characterized by a combination of point-group symmetries, such as reflection symmetry along the ($x = 0$ and $y = 0$) plane, rotational symmetry along the z -axis in the case of BiInO₃, and translation symmetry T_a by a fraction of the Bravais lattice vector \vec{a} . Repeated application of an n -fold Nonsymmorphic symmetry results in the translation of Bloch states $n-1$ times, expressed as:

$$\mathcal{G}^n = \{g^n | nt\} = \pm \mathcal{P} T_a, \quad \mathcal{P} \in 1, 2, \dots, n-1 \quad (1)$$

Here, g represents the n -fold point-group symmetry, T_a is the translation operator for the Bravais lattice vector, and the \pm sign on the right-hand side signifies Boson and Fermion states, respectively.

BiInO₃ exemplifies a material with Pna2₁ orthorhombic perovskite structure, falling under space group No.33. This material manifests various symmetries, including the Identity symmetry ($\mathbb{1}$) and Time reversal symmetry (\mathcal{T}), contributing to its unique topological characteristics. The following are the symmetries present in BiInO₃.

(1) Glide reflection Symmetry about yz -plane,

$$\{m_{100} | \frac{1}{2}\ \frac{1}{2}\ \frac{1}{2}\} : (x, y, z) \rightarrow (-x + \frac{1}{2}, y + \frac{1}{2}, z + \frac{1}{2}) \quad (2)$$

(2) Glide reflection Symmetry about the xz -plane,

$$\{m_{010} | \frac{1}{2}\ 0\ \frac{1}{2}\} : (x, y, z) \rightarrow (x + \frac{1}{2}, -y + \frac{1}{2}, z) \quad (3)$$

(3) Two-fold screw rotation symmetry about the z -axis,

$$\{2_{001} | 0\ 0\ \frac{1}{2}\} : (x, y, z) \rightarrow (-x, -y, z + \frac{1}{2}) \quad (4)$$

The crystallographic symmetry inherent in materials significantly influences their electronic structure. In the case of BiInO₃, the interplay between non-symmorphic symmetries and Spin-Orbit Interaction (SOI) is pivotal in determining the band structure, giving rise to phenomena such as band degeneracy and splitting. Our focus is understanding how specific symmetries, such as glide reflection symmetry and time reversal, contribute to forming Kramers-like degeneracy along distinct high symmetry paths in momentum space, as illustrated in Fig. 2(b). Before delving into the Eigenvalues and Eigenstates along these paths, it's necessary to comprehend how the glide reflection and time reversal operators act on the Bloch Eigenstates.

BiInO₃ is non-magnetic, preserving time inversion symmetry, which becomes a key aspect of our study. The time inversion operator, being antiunitary for Fermions, is a crucial element in understanding the band degeneracy and splitting along the chosen high symmetry path in the momentum space of this material. The time inversion operator is written as,

$$\mathcal{T} = i\sigma_y \hat{K} \quad (5)$$

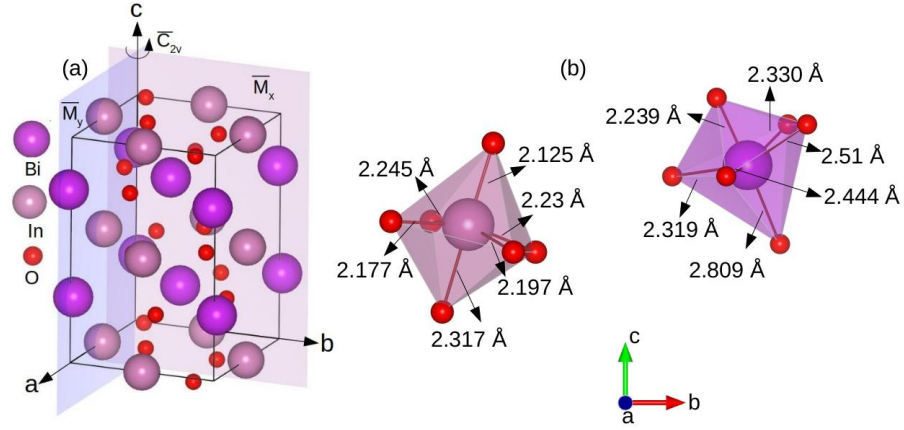


FIG. 1. (a) Crystal structure of BiInO₃ with symmetry planes. \tilde{M}_x is glide reflection plane about $x=0$ axis. \tilde{M}_y is glide reflection plane about $y=0$ axis and \tilde{C}_{2v} is screw rotational axis pointing along the c -axis. (b) The distorted In and Bi octahedra show the inequivalent bond length.

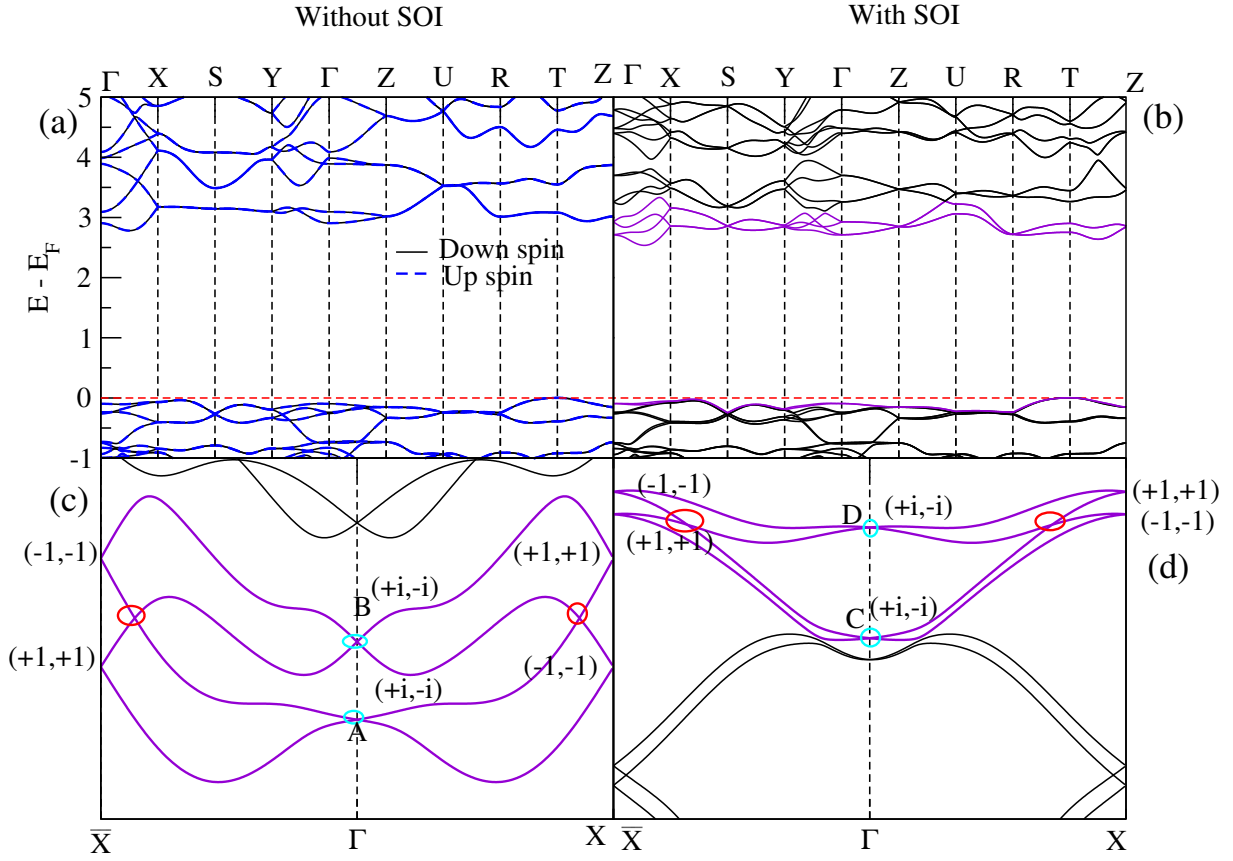


FIG. 2. Energy band structure and spin textures in BiInO₃. (a) and (b) show the bulk band structures of BiInO₃ without and with spin-orbit interaction (SOI), respectively. (c) illustrates the hourglass fermion network in the conduction band near the Γ point. The red circles mark the hourglass crossings, while the cyan circles indicate time-reversal invariant momenta (TRIMs). Points A and B on the energy axis at Γ represent states with a persistent spin texture pointing along the k_y direction. These states begin with eigenvalues $(+i, -i)$ and evolve toward the X point, ending with eigenvalues $(+1, +1)$ and $(-1, -1)$. (d) shows a similar hourglass fermion network in the valence band, close to the Fermi level, also centered at the Γ point. Here, points C and D indicate states with a Rashba-like spin texture. These also begin with eigenvalues $(+i, -i)$ and evolve toward X with final eigenvalues $(+1, +1)$ and $(-1, -1)$.

$$\mathcal{T}^2 = i^2 \sigma_y^2 \hat{\mathcal{K}}^2 = -\mathbb{1} \quad (6) \quad \text{where } \sigma_y \text{ Pauli spin matrix and } \hat{\mathcal{K}} \text{ is a complex conjuga-}$$

tion operator in Bloch State.

The time inversion operator commutes with all the space group transformations and considers spin-orbit interaction and all the space group symmetry also present in spin space. Let us define the time-spatial symmetries $\mathcal{T}\mathcal{M}_x = \mathcal{T}\{m_{100} | \frac{1}{2} \frac{1}{2} \frac{1}{2}\}$ and $\mathcal{T}\mathcal{M}_y = \mathcal{T}\{m_{010} | \frac{1}{2} 0 \frac{1}{2}\}$ also preserved in the crystal and particular section of momentum space. The Glide reflection symmetry, Time inversion symmetry and their product can operate on Bloch states having both crystal space and spin space. Operating the symmetry operator on position and spin space twice, we get the following equations,

$$\{m_{100}^2 | 0 1 1\} : (x, y, z) \rightarrow (x, y + 1, z + 1) i^2 \sigma_x^2 \quad (7)$$

$$\{m_{100}^2 | 0 1 1\} : (x, y, z) \rightarrow -e^{-i(k_y + k_z)}(x, y, z) \quad (8)$$

$$\{m_{010}^2 | 1 0 0\} : (x, y, z) \rightarrow (x + 1, y, z) i^2 \sigma_y^2 \quad (9)$$

$$\{m_{010}^2 | 1 0 0\} : (x, y, z) \rightarrow -e^{-ik_x}(x, y, z) \quad (10)$$

$$\mathcal{T}^2\{m_{100}^2 | 0 1 1\} : (x, y, z) \rightarrow e^{-i(k_y + k_z)}(x, y, z) \quad (11)$$

$$\mathcal{T}^2\{m_{010}^2 | 1 0 0\} : (x, y, z) \rightarrow e^{-ik_x}(x, y, z) \quad (12)$$

Let us redefine ψ to the Bloch state. From Eqs. (7) to (12) we can get eigenvalue equation of the symmetry operators as;

$$\left\{m_{100} \mid \frac{1}{2} \frac{1}{2} \frac{1}{2}\right\} \psi^\pm(\vec{k}) = \pm i e^{-i(k_y + k_z)/2} \psi^\pm(\vec{k}) \quad (13)$$

$$\left\{m_{010} \mid \frac{1}{2} 0 \frac{1}{2}\right\} \psi^\pm(\vec{k}) = \pm i e^{-ik_x/2} \psi^\pm(\vec{k}) \quad (14)$$

$$\mathcal{T} \left\{m_{100} \mid \frac{1}{2} \frac{1}{2} \frac{1}{2}\right\} \psi^\pm(\vec{k}) = \pm e^{-i(k_y + k_z)/2} \psi^\pm(\vec{k}) \quad (15)$$

$$\mathcal{T} \left\{m_{010} \mid \frac{1}{2} 0 \frac{1}{2}\right\} \psi^\pm(\vec{k}) = \pm e^{-ik_x/2} \psi^\pm(\vec{k}) \quad (16)$$

where eigenvalues are momentum-dependent and can be calculated to some constant, by knowing the value of momentum at a high symmetry point or path.

B. Electronic Structure of Bulk BiInO₃

A fascinating electronic structure has unfolded in our Density Functional Theory (DFT) calculations for both bulk and surface configurations of BiInO₃. Employing

the Berry phase method, we computed the Electric polarisation, revealing a substantial value of approximately 12.4 $\mu\text{C}/\text{cm}^2$ along the [001] direction. The crystal structure manifests distinct polar planes, with the BiO and InO₂ layers exhibiting positive and negative charge accumulation, respectively, forming a serial combination of conventional capacitors along the z-direction. BiInO₃ emerges as a band insulator with an indirect band gap of 2.77 eV without SOI. Upon introducing SOI into our calculations, a notable reduction in the band gap to 2.55 eV occurs, accompanied by a profound band-splitting phenomenon. In specific directions, exhibit protected band-splitting due to mirror glide reflection symmetry, forming a Kramer nodal line [35]. In some other particular directions, this led to the emergence of Weyl points facilitated by the exchange of Kramer pairs. Our symmetry analysis is used to understand the topological band structure of BiInO₃, which will be explained in the coming sections.

1. Symmetry analysis and Band structure

(A) Consider the high-symmetry path $\bar{X}(-\pi, 0, 0) \rightarrow \Gamma(0, 0, 0) \rightarrow X(\pi, 0, 0)$, along which a general momentum point $(k_x, 0, 0)$ with $-\pi/a \leq k_x \leq \pi/a$ traces the trajectory. The little group along this path is composed of two key symmetries: the glide reflection $\{m_{010} | \frac{1}{2} 0 \frac{1}{2}\}$ (in the xz-plane) and the antiunitary symmetry $\mathcal{T}\{m_{100} | \frac{1}{2} \frac{1}{2} \frac{1}{2}\}$ (involving time-reversal and a glide along the yz-plane). These symmetries preserve k_x along the path. As derived from Eq. (14), the eigenvalues of the glide operator $\{m_{010} | \frac{1}{2} 0 \frac{1}{2}\}$ vary along the path: at Γ they are $(+i, -i)$, at X they become $(+1, -1)$, and at $-\bar{X}$ they are $(-1, +1)$. Although ζ contains time-reversal symmetry, we find from the relation $\mathcal{T}^2\{m_{100}^2 | 0 1 1\}$ that Kramers degeneracy is not enforced along this path. Consequently, the bands split away from the TRIM points, which are Γ and X . However, at the TRIM points themselves, degeneracy is protected. This results in an hourglass-shaped band structure, where partner-switching within the symmetry-enforced eigenvalue pairs causes a band crossing at least once between Γ and X [36–38]. As illustrated in Fig. 2(c) and Fig. 2(d), such hourglass dispersion appears at 2.99 eV in the conduction band and at -0.094 eV in the valence band, respectively.

(B) Next, we consider the high-symmetry path $X(\pi, 0, 0) \rightarrow S(\pi, \pi, 0)$, where the momentum varies as $(\pi, k_y, 0)$ with $0 \leq k_y \leq \pi/b$. Along this path, the symmetries $\{m_{100} | \frac{1}{2} \frac{1}{2} \frac{1}{2}\}$ and $\mathcal{T}\{m_{010} | \frac{1}{2} 0 \frac{1}{2}\}$ form the little group, as k_y remains invariant under both. From Eq. (12), we find that $\{m_{010}^2 | 1 0 0\} = -\mathbb{1}$, indicating that time-reversal symmetry enforces Kramers degeneracy. Thus, the bands appear as pairs $(\psi, \mathcal{T}\{m_{010} | \frac{1}{2} 0 \frac{1}{2}\}\psi)$, which are degenerate along the path. Since the crystal Hamiltonian commutes with these symmetries and is invariant under time reversal, the Bloch states are also eigenstates of $\{m_{100} | \frac{1}{2} \frac{1}{2} \frac{1}{2}\}$.

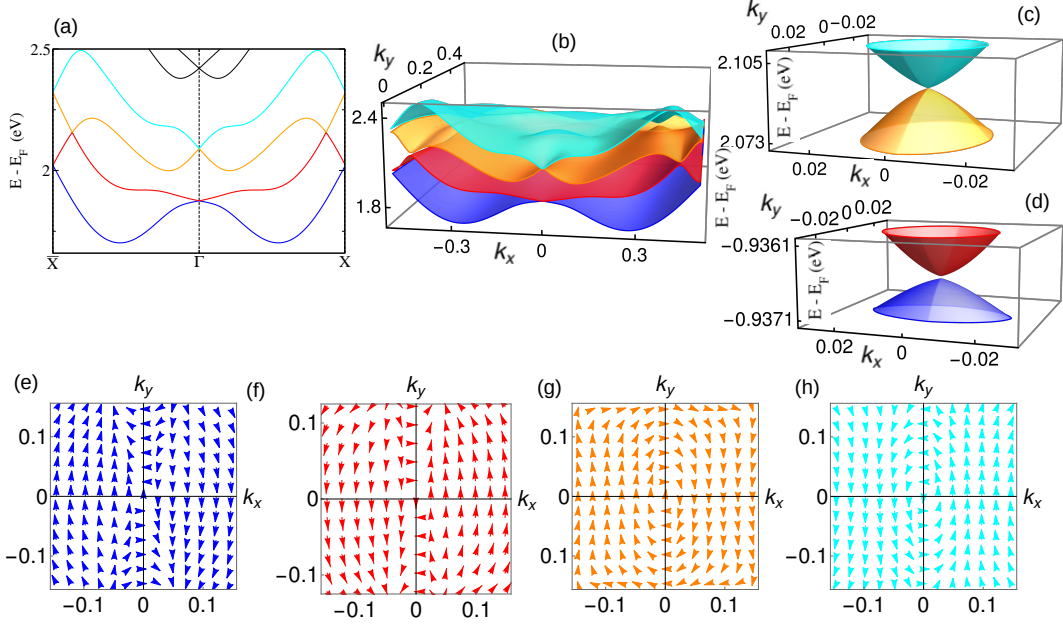


FIG. 3. (a) Hourglass band network formed by the lowest four conduction bands of bulk BiInO₃ along the high-symmetry path $\bar{X} \rightarrow \Gamma \rightarrow X$, where Kramers pairs exchange their partners as the path proceeds from Γ to X . (b) Cross-sectional view of the corresponding 3D band structure. (c) and (d) Three-dimensional band structures focused on a narrow energy window around the Γ point. (e)–(h) Persistent spin textures of the four conduction bands shown in (a), calculated using the first-principles DFT method. The colour of the spin corresponds to the colour of the band in (a).

According to Eq. (13), we can write the eigenvalue equations as $\{m_{100} | \frac{1}{2} \frac{1}{2} \frac{1}{2}\} \psi^\pm(\vec{k}) = \pm \psi^\pm(\vec{k})$, and similarly, $\{m_{100} | \frac{1}{2} \frac{1}{2} \frac{1}{2}\} (\mathcal{T} \{m_{010} | \frac{1}{2} 0 \frac{1}{2}\} \psi^\pm(\vec{k})) = \pm (\mathcal{T} \{m_{010} | \frac{1}{2} 0 \frac{1}{2}\} \psi^\pm(\vec{k}))$. As a result, the bands appear as two symmetry-protected Kramers doublets: $(\psi^+, \mathcal{T} \{m_{010} | \frac{1}{2} 0 \frac{1}{2}\} \psi^+)$ and $(\psi^-, \mathcal{T} \{m_{010} | \frac{1}{2} 0 \frac{1}{2}\} \psi^-)$.

(C) Consider now the high-symmetry path $S(\pi, \pi, 0) \rightarrow Y(0, \pi, 0)$, where the momentum vector is $(k_x, \pi, 0)$ with $0 \leq k_x \leq \pi/a$. Along this segment, the relevant symmetries are again $\{m_{010} | \frac{1}{2} 0 \frac{1}{2}\}$ and $\mathcal{T} \{m_{100} | \frac{1}{2} \frac{1}{2} \frac{1}{2}\}$, which preserve \vec{k} and hence form the little group. This is similar to the $\Gamma \rightarrow X$ segment discussed earlier. Here too, $\mathcal{T}^2 \{m_{100}^2 | 0 1 1\} = -\mathbb{1}$, enforcing Kramers degeneracy. The bands are therefore doubly degenerate along the path, forming Kramers pairs $(\psi(\vec{k}), \mathcal{T} \{m_{010} | \frac{1}{2} 0 \frac{1}{2}\} \psi(\vec{k}))$ called Kramers nodal line[39].

(D) Lastly, we consider the path from $Y(0, \pi, 0) \rightarrow \Gamma(0, 0, 0)$, where the momentum varies as $(0, k_y, 0)$ with $0 \leq k_y \leq \pi/b$. The little group here includes $\{m_{100} | \frac{1}{2} \frac{1}{2} \frac{1}{2}\}$ and $\mathcal{T} \{m_{010} | \frac{1}{2} 0 \frac{1}{2}\}$, which again preserves k_y along the path. This is similar in symme-

try structure to the $X \rightarrow S$ path. However, in this case, Eq. (13) gives $\mathcal{T}^2 \{m_{010}^2 | 1 0 0\} = \mathbb{1}$, which does not enforce Kramers degeneracy. The eigenvalues of $\{m_{100} | \frac{1}{2} \frac{1}{2} \frac{1}{2}\}$ are $(+i, -i)$ at the Γ point, and $(+1, -1)$ at Y . Because the eigenvalues change between the endpoints, the bands split along the path and must cross at least once due to partner switching. This again results in an hourglass-shaped dispersion along the $Y \rightarrow \Gamma$ direction.

2. $\vec{k} \cdot \vec{p}$ Hamiltonian

The energy band splitting and their spin texture in BiInO₃ at Γ point can be understood by writing the $\vec{k} \cdot \vec{p}$ Hamiltonian considering all the symmetries present. The point group symmetry at Γ point is C_{2v} characterized by two-fold rotation about z-axis ($C_{2z} \{2_{001} | 0 0 0\}$), reflection about xz-plane ($\mathcal{M}_y \{m_{010} | 0 0 0\}$) and reflection about yz-plane ($\mathcal{M}_x \{m_{100} | 0 0 0\}$). BiInO₃ is non-magnetic, thus preserving time-reversal symmetry (\mathcal{T}). The time-reversal symmetry reverses the direction of spinor $\vec{\sigma} \rightarrow -\vec{\sigma}$ and velocity $\vec{k} \rightarrow -\vec{k}$. Symmetries play a crucial role in understanding transformations of

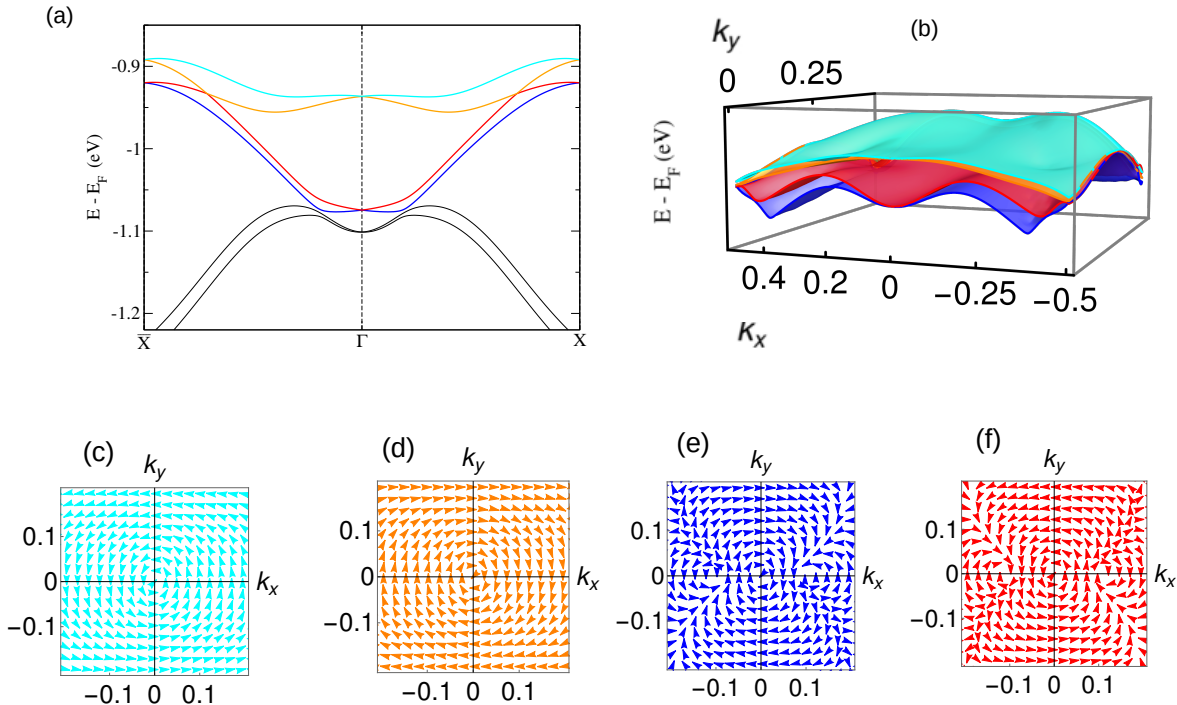


FIG. 4. (a) Hourglass band network formed by the highest four valence bands of bulk BiInO₃ along the high-symmetry path $\bar{X} \rightarrow \Gamma \rightarrow X$, where Kramers pairs exchange their partners as the path proceeds from Γ to X . (b) Three-dimensional band structures focused on a narrow energy window around the Γ point. (c)–(f) Persistent spin textures of the four valence bands shown in (a), calculated using the first-principles DFT method. The colour of the spin corresponds to the colour of the band in (a)

TABLE I. Transformation rules for the wave vector \vec{k} and spin $\vec{\sigma}$ under the C_{2v} point group symmetry operations at the $\Gamma(0,0,0)$ point in the Brillouin zone of BiInO₃. The wave vector \vec{k} is defined relative to the high-symmetry Γ point. Here, \hat{K} represents the complex conjugation operator.

Symmetry	Wave vector (\vec{k})	Spin (σ)	Invariant	
			Linear	Cubic
$\mathcal{T} = i\sigma_y \hat{K}$	$(-k_x, -k_y, -k_z)$	$(-\sigma_x, -\sigma_y, -\sigma_z)$	$k_i \sigma_i, i = x, y, z$	$k_i^3 \sigma_i, i = x, y, z$
$\{m_{100} \mid \frac{1}{2} \frac{1}{2} \frac{1}{2}\}$	$(-k_x, k_y, k_z)$	$(\sigma_x, -\sigma_y, -\sigma_z)$	$k_x \sigma_y, k_x \sigma_z, k_y \sigma_x, k_z \sigma_x$	$k_x^3 \sigma_y, k_x^3 \sigma_z, k_y^3 \sigma_x, k_z^3 \sigma_x$
$\{m_{010} \mid \frac{1}{2} 0 \frac{1}{2}\}$	$(k_x, -k_y, k_z)$	$(-\sigma_x, \sigma_y, -\sigma_z)$	$k_x \sigma_y, k_y \sigma_x, k_y \sigma_z$	$k_x^3 \sigma_y, k_y^3 \sigma_x, k_y^3 \sigma_z$
$\{2_{001} \mid 0 0 \frac{1}{2}\}$	$(-k_x, -k_y, k_z)$	$(-\sigma_x, -\sigma_y, \sigma_z)$	$k_z \sigma_z, k_i \sigma_i, i = x, y$	$k_z^3 \sigma_z, k_i^3 \sigma_i, i = x, y$

spin vectors on the Bloch sphere. The rotation of the Bloch sphere around an arbitrary axis, denoted by \hat{n} , is mathematically captured by the rotation matrix $R_{\hat{n}}(\theta) = e^{-i\frac{1}{2}\theta\hat{n}\cdot\vec{\sigma}}$ [40, 41]. This matrix transforms the Pauli spin matrices as $\sigma'_i = R(\theta)\sigma_i R(\theta)^{-1}$, where i can be x, y , or z . In the $\{2_{001} \mid 0 0 \frac{1}{2}\}$ symmetry, represented by $i\sigma_z$, the spinor on the XY -plane of the Bloch sphere undergoes a unique transformation: $(\sigma_x, \sigma_y, \sigma_z) \rightarrow (-\sigma_x, -\sigma_y, \sigma_z)$.

When a quantum spinor (such as a Pauli spin vector) is subjected to consecutive mirror reflections, the resulting operation is mathematically equivalent to a rotation. Specifically, two successive reflections about orthogonal mirror planes correspond to a 180° rotation around the axis perpendicular to the plane defined by those mirrors. This concept, rooted in symmetry composition, plays a vital role in analysing spin textures.

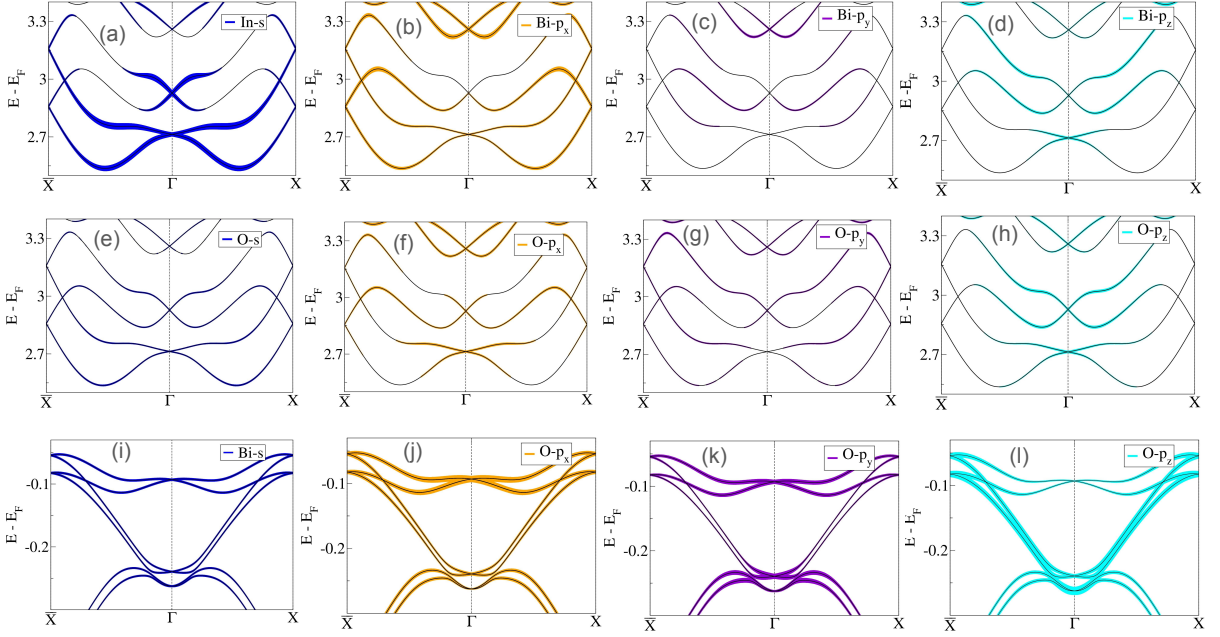


FIG. 5. (a)–(h) Orbital-projected hourglass fermion band structures near the conduction band minimum. These bands exhibit a Persistent Spin Texture (PST) directed along the k_y -axis, primarily due to dominant contributions from In- s , Bi- p_x , and O- p_y orbitals. (i)–(p) Orbital-projected hourglass fermion band structures near the Fermi energy around the Γ point. These bands display Rashba-type spin texture, originating from the dominant contribution of O- p_x and O- p_y orbitals.

In spin systems, a mirror reflection about the XZ-plane ($\{m_{010} | 0 0 0\}$) corresponds to a 180° rotation about the y -axis and is represented by the operator $i\sigma_y$. Under this transformation, the Pauli matrices transform as $(\sigma_x, \sigma_y, \sigma_z) \rightarrow (-\sigma_x, \sigma_y, -\sigma_z)$, preserving σ_y and flipping σ_x and σ_z . Similarly, a mirror reflection about the YZ-plane ($\{m_{100} | 0 0 0\}$) corresponds to a 180° rotation about the x -axis, represented by $i\sigma_x$, which transforms the spin components as $(\sigma_x, \sigma_y, \sigma_z) \rightarrow (\sigma_x, -\sigma_y, -\sigma_z)$. These transformation rules are crucial for constructing effective $\vec{k} \cdot \vec{p}$ Hamiltonians in crystals with spin-orbit interaction, as they determine the allowed and forbidden spin terms under specific point-group symmetries. The complete transformation properties of wavevector \vec{k} and spin $\vec{\sigma}$ under the relevant symmetry operations are summarised in Table I.

Since BiInO₃ is a non-symorphic and non-magnetic material, spin splitting is observed due to spin-orbit interaction. The $\vec{k} \cdot \vec{p}$ Hamiltonian of the crystal is written using the theory of invariant [42, 43] as below,

$$\mathcal{H} = \mathcal{H}_o + \mathcal{H}_{so} \quad (17)$$

Where,

$$\mathcal{H}_o = -\hbar \left(\frac{1}{2m_x} \frac{\partial^2}{\partial x^2} + \frac{1}{2m_y} \frac{\partial^2}{\partial y^2} \right) \quad (18)$$

The SOI term of the Hamiltonian \mathcal{H}_{so} is the sum of the product of Pauli matrices and the wavevector component transforming similarly under the symmetry present

in the crystal. From the table, $k_x \rightarrow -k_x$ and $\sigma_y \rightarrow -\sigma_y$ under all the symmetries except M_y , where $k_x \rightarrow k_x$ and $\sigma_y \rightarrow \sigma_y$ on multiplying them, we get $k_x \sigma_y$, which is invariant under all the crystal symmetries and time-reversal symmetry. Thus, in a similar way of collecting the linear and cubic invariant terms under all the symmetries, we get \mathcal{H}_{so} ,

$$\begin{aligned} \mathcal{H}_{so} = & \alpha_1 k_x \sigma_y + \alpha_2 k_y \sigma_x + \beta_1 k_x^3 \sigma_y + \beta_2 k_y^3 \sigma_x \\ & + \beta_3 k_x^2 k_y \sigma_x + \beta_4 k_y^2 k_x \sigma_y \end{aligned} \quad (19)$$

The point group of BiInO₃ is C_{2v} , which belongs to the gyrotropic point group and allows only linear wavevector splitting[44]. Considering only the linear terms, the Hamiltonian becomes.

$$\mathcal{H}_{so} = \alpha_1 k_x \sigma_y + \alpha_2 k_y \sigma_x \quad (20)$$

Rewriting the Eq. (20) as[45],

$$\mathcal{H}_{so} = \alpha_R (k_x \sigma_y + k_y \sigma_x) + \alpha_D (k_x \sigma_y - k_y \sigma_x) \quad (21)$$

where $\alpha_R = \frac{\alpha_1 + \alpha_2}{2}$ and $\alpha_D = \frac{\alpha_1 - \alpha_2}{2}$.

The second part of the Hamiltonian is the Rashba Hamiltonian equal to $\alpha_R (\vec{k} \times \vec{\sigma})|_{z=0}$, and the first part of the Hamiltonian is the Dresselhaus Hamiltonian[17]. α_R and α_D are the Rashba and Dresselhaus SOI constants, respectively.

The band-energy of Eq. (17) can be written as,

$$\varepsilon^\pm(k) = \frac{k_x^2}{2m_x} + \frac{k_y^2}{2m_y} \pm \sqrt{\alpha_1^2 k_x^2 + \alpha_2^2 k_y^2} \quad (22)$$

TABLE II. Character table for the C_{2v} point group.

IR	$\mathbb{1}$	C_2	\mathcal{M}_x	\mathcal{M}_y	Linear	Quadratic	Rotation
A_1	1	1	1	1	z	x^2, y^2, z^2	
A_2	1	1	-1	-1		xy	σ_z
B_1	1	-1	1	-1	x	xz	σ_y
B_2	1	-1	-1	1	y	yz	σ_x

The eigenstate of the Eq. (17) can be written in spinor form as,

$$\psi^\pm(k) = \frac{1}{\sqrt{2}}(\pm\xi|\uparrow\rangle + |\downarrow\rangle) \quad (23)$$

Where,

$$\xi = \frac{\sqrt{\alpha_1^2 \cos^2 \phi + \alpha_2^2 \sin^2 \phi}}{i\alpha_1 \cos \phi + \alpha_2 \sin \phi} \quad (24)$$

$|\uparrow\rangle$ and $|\downarrow\rangle$ are the spinors for electrons spinning up and down, respectively, and ϕ is the angle between the spin and the k_z axis.

The symmetry allowed expectation value of spin operator is $s^\pm = \frac{1}{2} \langle \psi^\pm(k) | \sigma | \psi^\pm(k) \rangle$ results,

$$\langle s_x \rangle^\pm = \frac{1}{2} \left(\frac{\pm\alpha_2 \sin \phi}{\sqrt{\alpha_1^2 \cos^2 \phi + \alpha_2^2 \sin^2 \phi}} \right) \quad (25)$$

$$\langle s_y \rangle^\pm = \frac{1}{2} \left(\frac{\pm\alpha_1 \cos \phi}{\sqrt{\alpha_1^2 \cos^2 \phi + \alpha_2^2 \sin^2 \phi}} \right) \quad (26)$$

$$\langle s_z \rangle^\pm = 0 \quad (27)$$

C. Spin Textue

In our study, we utilised the DFT, $\vec{k} \cdot \vec{p}$ model, and group theory to analyse the spin texture of the energy band near the Γ point in momentum space. We observed that two pairs of bands between Γ and X point shared Kramer partners, influenced by the symmetries along the high symmetry path, which glue up the band between the high symmetry points. The band's double degeneracy at high symmetry points Γ and X is due to time reversal symmetry. From Fig. 4, we can see the up-down-down-up spin arrangement of the hourglass bands. The direction of the spin arrangement of the hourglass is governed by the symmetry at the high symmetry path. Specifically, at Γ point both mirror plane $\{m_{010} | \frac{1}{2} 0 \frac{1}{2}\}$ and $\{m_{100} | \frac{1}{2} \frac{1}{2} \frac{1}{2}\}$ intersect to each other. Both $\{m_{010} | \frac{1}{2} 0 \frac{1}{2}\}$ and $\{m_{100} | \frac{1}{2} \frac{1}{2} \frac{1}{2}\}$ mirror symmetries keep the Γ point invariant, and the crystal

Hamiltonian commutes with both these symmetries. As a result, the direction of the spin at the Γ point is determined by this symmetry. $\{m_{010} | \frac{1}{2} 0 \frac{1}{2}\}$ leaves σ_y invariant while flipping the direction of σ_x and σ_z . Consequently, $\langle \sigma_x \rangle$ and $\langle \sigma_z \rangle$ are zero, while $\langle \sigma_y \rangle$ non-zero. Similarly, for $\{m_{100} | \frac{1}{2} 0 \frac{1}{2}\}$ $\langle \sigma_y \rangle$ and $\langle \sigma_z \rangle$ are zero. In contrast, $\langle \sigma_x \rangle$ is non-zero. $\langle \sigma_y \rangle$ and $\langle \sigma_z \rangle$ are calculated in Eqs. (25) to (27) using $\vec{k} \cdot \vec{p}$ hamiltonian.

1. Spin Texture of Valance band hourglass fermion network at Γ point

After fitting the $\vec{k} \cdot \vec{p}$ model to the DFT results around point C of 2(d), we determined that $\alpha_1 = 0.06$ and $\alpha_2 = -0.06$, yielding Dresselhaus SOI constant $\alpha_D = 0$ and Rashba SOI constant $\alpha_R = 0.12$. Consequently, the spin of the hourglass fermion exhibits a Rashba spin texture. Similarly, at point D of Fig. 2(d), we obtained $\alpha_1 = 0.01$ and $\alpha_2 = -0.01$, resulting in Dresselhaus SOI constant $\alpha_D = 0$ and Rashba SOI constant $\alpha_R = 0.02$. This illustrates that Rashba SOI effectively suppresses Dresselhaus SOI, leading to a Rashba spin texture. The corresponding spin texture is shown in Fig. 4 To understand the spin texture, we examine the invariant of the basis function of the orbitals contributing to the band [26]. The point group at the Γ point is C_{2v} , with its character table displayed in Table II. In our analysis of the orbital contribution to the energy band, we plotted the orbital projected band for the hourglass fermions in Fig. 5. We observe that O- p_x and O- p_y orbitals make equal contributions, surpassing those from O- p_z . Referring to Table II, we note that O- p_x and σ_y follow the B_1 representation, which is not invariant under $\{2_{001} | 0 0 0\}$ and $\{m_{010} | 0 0 0\}$, but is invariant under $\{m_{100} | 0 0 0\}$. Conversely, O- p_y and σ_x follow the B_2 representation, which is not invariant under $\{2_{001} | 0 0 0\}$ and $\{m_{100} | 0 0 0\}$, but invariant under $\{m_{010} | 0 0 0\}$. Given the nearly equal contributions of O- p_x and O- p_y , the spin direction is governed by the expectation of both σ_x and σ_y . This results in a Rashba spin texture, consistent with the DFT-calculated spin texture and the $\vec{k} \cdot \vec{p}$ model.

2. Spin texture of conduction band hourglass fermion network at Γ point

The conduction band minimum lies between the Γ and X points at 2.53eV. This minimum is one of the bands among a set of four bands contributing to the formation of the Hourglass band dispersion. We calculated the spin texture for the four bands, as shown in Fig. 4. Upon fitting the $\vec{k} \cdot \vec{p}$ model with DFT results at point A of Fig. 2(c), we determined $\alpha_1 = 0.195$ and $\alpha_2 = -0.01$. We calculated the Rashba and Dresselhaus spin-orbit interaction (SOI) constants from these values, yielding

$\alpha_R = 0.196$ for Rashba SOI and $\alpha_D = 0.194$ for Dresselhaus SOI. Remarkably, these constants are nearly equal, resulting in a momentum-independent spin texture point along the k_y direction, referred to as Persistent Spin Texture (PST). Similarly, at point B of Fig. 2(c), the equality of α_1 and α_2 values also gives rise to PST. Consequently, the spin polarisation of the Hourglass Fermion along the Γ to X direction is arranged as up-down-down-up along the k_y direction. On the other hand, the spin texture of the valence band around the Γ point at points C and D exhibits a Rashba spin texture, with equal contributions from σ_x and σ_y , consistent with symmetry analysis, DFT, and $\vec{k} \cdot \vec{p}$ model predictions. However, the spin texture of the conduction band differs significantly from that of the valence band, despite both bands sharing the same C_{2v} point group present at the Γ point. Given that the spin texture points along the k_y direction, the expectation value of σ_x is nearly zero. Understanding a clear picture of the spin texture necessitates examining the competition of orbital characters in the bands. Fig. 5 illustrates the orbital-projected bands, revealing that in hourglass fermions, the dominant orbital characters originate from In-s, Bi- p_x , and O- p_x orbitals, compared to the contributions from Bi- p_y and O- p_y . The p_x orbital of Bi and O follows the B_1 representation, while the p_y orbital of Bi and O follows the B_2 representation. Notably, the rotational part σ_y follows the B_1 representation, whereas σ_x follows the B_2 representation. As the linear basis function following the B_1 representation dominates over that following the B_2 representation, σ_y surpasses σ_x , resulting in the spins of hourglass fermions aligning along the k_y direction.

IV. CONCLUSION

In this research, we investigated the electronic structure of semiconducting bulk BIO within the framework of density-functional theory, including spin-orbit interaction. The study provides insights into how the nonsymmorphic crystal symmetries of BIO, such as glide reflection symmetry, impact its energy band structure. BIO exhibits an hourglass fermion attributed to its nonsymmorphic crystal symmetries. The interplay between the SOI and point group symmetry at the Γ point results in unique spin-momentum locking in the band near the Fermi energy, and results in Rashba spin texture at Γ point below the Fermi energy and PSH above the Fermi energy at Γ high symmetry point. Though both bands share the same point group symmetry, they feature two different types of spin-texture due to the competition of p-orbital character of constituent atoms in the bands. Below the Γ -point we find Rashba spin-texture due to equal contribution coming from O- p_x and O- p_y , and above Γ -point there is PSH along the y-direction as Bi- p_x and O- p_x is dominating. The direction of spin-texture is also calculated using $\vec{k} \cdot \vec{p}$ method, which matches with the DFT result. The unique spin textures in BIO, driven by symmetry-enforced mechanisms, hold significant potential for spintronics applications. The PST in the conduction band is particularly advantageous for developing reliable and efficient spin field-effect transistors (spin-FETs) by minimising spin relaxation challenges[22, 23].

ACKNOWLEDGMENTS

RK acknowledges UGC, India, for a research fellowship through grant number 1500/(CSIR-UGC NET JUNE 2017). NG acknowledges financial support from SERB, India, through grant number CRG/2021/005320. The use of high-performance computing facilities at IISER Bhopal is gratefully acknowledged.

-
- [1] C. L. Kane and E. J. Mele, Quantum Spin hall effect in graphene, *Physical Review Letters* **95**, 1 (2005).
 - [2] J. E. Moore and L. Balents, Topological invariants of time-reversal-invariant band structures, *Physical Review B - Condensed Matter and Materials Physics* **75**, 3 (2007).
 - [3] L. Fu and C. L. Kane, Time reversal polarization and a Z2 adiabatic spin pump, *Physical Review B - Condensed Matter and Materials Physics* **74**, 1 (2006).
 - [4] C. K. Chiu, J. C. Teo, A. P. Schnyder, and S. Ryu, Classification of topological quantum matter with symmetries, *Reviews of Modern Physics* **88**, 1 (2016).
 - [5] L. Fu and C. L. Kane, Topological insulators with inversion symmetry, *Physical Review B - Condensed Matter and Materials Physics* **76**, 1 (2007).
 - [6] Z. Wang, A. Alexandradinata, R. J. Cava, and B. A. Bernevig, Hourglass fermions, *Nature* **532**, 189 (2016).
 - [7] S. Li, Y. Liu, S. Wang, Z. Yu, S. Guan, X. Sheng, and Y. Yao, Nonsymmorphic-symmetry-protected hourglass dirac loop, nodal line, and dirac point in bulk and monolayer (= ta, nb), *Physical Review B* **97**, 045131 (2018).
 - [8] S. S. Wang, Y. Liu, Z. M. Yu, X. L. Sheng, and S. A. Yang, Hourglass Dirac chain metal in rhenium dioxide, *Nature Communications* **8**, 1 (2017).
 - [9] Z. F. Wang, B. Liu, and W. Zhu, Hourglass Fermion in Two-Dimensional Material, *Physical Review Letters* **123**, 126403 (2019).
 - [10] Y. Xu and L.-M. Duan, Type-ii weyl points in three-dimensional cold-atom optical lattices, *Phys. Rev. A* **94**, 053619 (2016).

- [11] A. Soluyanov, D. Gresch, Z. Wang, Q. Wu, M. Troyer, X. Dai, and B. Bernevig, Type-II Weyl semimetals, *Nature* **527**, 495 (2015).
- [12] K. Zhang and G. Volovik, Lifshitz transitions via the type-II Dirac and type-II Weyl points, *JETP Letters* **105**, 675 (2017).
- [13] B. Rosenstein, B. Shapiro, D. Li, and I. Shapiro, Magnetic properties of type-I and type-II Weyl semimetals in the superconducting state, *Physical Review B* **97**, 144510 (2018).
- [14] M. Yao, N. Xu, Q. Wu, G. Autès, N. Kumar, and V. Strocov, Observation of Weyl nodes in robust type-II Weyl semimetal, *Physical Review Letters* **122**, 176402 (2019).
- [15] K. Shiozaki, M. Sato, and K. Gomi, Topology of nonsymmorphic crystalline insulators and superconductors, *Phys. Rev. B* **93**, 195413 (2016).
- [16] J. Ma, C. Yi, B. Lv, Z. Wang, S. Nie, L. Wang, L. Kong, Y. Huang, P. Richard, P. Zhang, K. Yaji, K. Kuroda, S. Shin, H. Weng, B. A. Bernevig, Y. Shi, T. Qian, and H. Ding, Experimental evidence of hourglass fermion in the candidate nonsymmorphic topological insulator KHgSb , *Science Advances* **3**, 2 (2017).
- [17] V. E. 100, N. B. Er, and G. Dresselhaus, Spin-Orbit Coupling Effects in Zinc Blende Structures, *Phys. Rev. Phys. Rev.* *Phys. Rev.* **96**, 280 (1954).
- [18] E. I. Rashba, Properties of semiconductors with an extremum loop. 1. Cyclotron and combinational resonance in a magnetic field perpendicular to the plane of the loop, *Sov. Phys. Solid State* **2**, 1109 (1960).
- [19] E. I. Rashba, Properties of semiconductors with an asymmetry in the spatial distribution of the charge carriers, *Soviet Physics - Solid State* **2**, 1109 (1960).
- [20] Y. A. Bychkov and E. I. Rashba, Oscillatory effects and the magnetic susceptibility of carriers in inversion layers, *Journal of Physics C: Solid State Physics* **17**, 6039 (1984).
- [21] E. I. Rashba, Spin-orbit interaction in a semiconductor with structural inversion asymmetry, *Physical Review* **140**, 76 (1965).
- [22] S. Datta and B. Das, Electronic analog of the electro-optic modulator, *Applied Physics Letters* **56**, 665 (1990).
- [23] M. I. Dyakonov, ed., *Spin Physics in Semiconductors*, Springer Series in Solid-State Sciences, Vol. 157 (Springer, Cham, Switzerland, 2017).
- [24] J. D. Koralek and et al., Emergence of the persistent spin helix in semiconductor quantum wells, *Nature* **458**, 610 (2009).
- [25] J. Schliemann, Colloquium: Persistent spin textures in semiconductor nanostructures, *Reviews of Modern Physics* **89**, 1 (2017).
- [26] S. Bandyopadhyay and I. Dasgupta, Orbital-dependent spin textures in ferroelectric Rashba systems, *Physical Review B* **103**, 1 (2021).
- [27] A. A. Belik, S. Y. Stefanovich, B. I. Lazoryak, and E. Takayama-Muromachi, BiInO_3 : A polar oxide with GdFeO_3 -type perovskite structure, *Chemistry of Materials* **18**, 1964 (2006).
- [28] P. E. Blöchl, Projector augmented-wave method, *Phys. Rev. B* **50**, 17953 (1994).
- [29] G. Kresse and J. Furthmüller, Efficient iterative schemes for ab initio total-energy calculations using a plane-wave basis set, *Physical Review B* **54**, 11169 (1996).
- [30] G. Kresse and D. Joubert, From ultrasoft pseudopotentials to the projector augmented-wave method, *Physical Review B* **59**, 1758 (1999).
- [31] J. P. Perdew, K. Burke, and M. Ernzerhof, Generalized Gradient Approximation Made Simple, *Phys. Rev. Lett.* **77**, 3865 (1996).
- [32] P. E. Blöchl, O. Jepsen, and O. K. Andersen, Improved tetrahedron method for Brillouin-zone integrations, *Phys. Rev. B* **49**, 16223 (1994).
- [33] P. Blaha, K. Schwarz, F. Tran, R. Laskowski, G. K. H. Madsen, and L. D. Marks, Wien2k: An apw+lo program for calculating the properties of solids, *The Journal of Chemical Physics* **152**, 074101 (2020), https://pubs.aip.org/aip/jcp/article-pdf/doi/10.1063/1.5143061/16727313/074101_1_online.pdf.
- [34] S. Ahmed, J. Kivinen, B. Zaporzan, L. Curiel, S. Pichardo, and O. Rubel, BerryPI: A software for studying polarization of crystalline solids with WIEN2k density functional all-electron package, *Computer Physics Communications* **184**, 647 (2013).
- [35] Y. M. Xie, X. J. Gao, X. Y. Xu, C. P. Zhang, J. X. Hu, J. Z. Gao, and K. T. Law, Kramers nodal line metals, *Nature Communications* **12**, 1 (2021).
- [36] L. Wang, S.-K. Jian, and H. Yao, Hourglass semimetals with nonsymmorphic symmetries in three dimensions, *Phys. Rev. B* **96**, 075110 (2017).
- [37] Y. X. Zhao and A. P. Schnyder, Nonsymmorphic symmetry-required band crossings in topological semimetals, *Phys. Rev. B* **94**, 195109 (2016).
- [38] R.-Y. Liu, A. Huang, R. Sankar, J. A. Hlevyack, C.-C. Su, S.-C. Weng, M.-K. Lin, P. Chen, C.-M. Cheng, J. D. Denlinger, S.-K. Mo, A. V. Fedorov, C.-S. Chang, H.-T. Jeng, T.-M. Chuang, and T.-C. Chiang, Dirac nodal line in hourglass semimetal $\text{Nb}_3\text{Sb}_2\text{Te}_6$, *Nano Letters* **23**, 380 (2023).
- [39] Y.-M. Xie, X.-J. Gao, X. Y. Xu, C.-P. Zhang, J.-X. Hu, J. Z. Gao, and K. T. Law, Kramers nodal line metals, *Nature Communications* **12**, 3064 (2021).
- [40] W. L. Bade and H. Jehle, An Introduction to Spinors, *Reviews of Modern Physics* **25**, 714 (1953), [arXiv:1312.3824](https://arxiv.org/abs/1312.3824).
- [41] A. M. Steane, An introduction to spinors (2013), [arXiv:1312.3824 \[math-ph\]](https://arxiv.org/abs/1312.3824).
- [42] G. L. B. G. E. Pikus, *Symmetry and strain-induced effects in semiconductors* (Wiley, 1974).
- [43] R. Winkler, Conclusions., Springer, 278 (2003).
- [44] S. D. Ganichev and L. E. Golub, Interplay of Rashba/Dresselhaus spin splittings probed by photogalvanic spectroscopy - A review, *Physica Status Solidi (B) Basic Research* **251**, 1801 (2014).
- [45] L. L. Tao, T. R. Paudel, A. A. Kovalev, and E. Y. Tsymbal, Reversible spin texture in ferroelectric HfO_2 , *Physical Review B* **95**, 1 (2017).